Received: 20 January 2021 | Revised: 22 March 2021 | Accepted: 7 May 2021

DOI: 10.1002/nme.6744

RESEARCH ARTICLE

WILEY

Modeling and discretization of flow in porous media with thin, full-tensor permeability inclusions

Michele Starnoni[1,2] | **Inga Berre**[1] | **Eirik Keilegavlen**[1] | **Jan Martin Nordbotten**[1]

[1]Department of Mathematics, University of Bergen, Bergen, Norway

[2]Department of Environment, Land and Infrastructure Engineering, Politecnico di Torino, Torino, Italy

Correspondence
Michele Starnoni, Department of Mathematics, University of Bergen, Bergen, Norway.
Email: michele.starnoni@polito.it

Abstract

When modeling fluid flow in fractured reservoirs, it is common to represent the fractures as lower-dimensional inclusions embedded in the host medium. Existing discretizations of flow in porous media with thin inclusions assume that the principal directions of the inclusion permeability tensor are aligned with the inclusion orientation. While this modeling assumption works well with tensile fractures, it may fail in the context of faults, where the damage zone surrounding the main slip surface may introduce anisotropy that is not aligned with the main fault orientation. In this article, we introduce a generalized dimensional reduced model which preserves full-tensor permeability effects also in the out-of-plane direction of the inclusion. The governing equations of flow for the lower-dimensional objects are obtained through vertical averaging. We present a framework for discretization of the resulting mixed-dimensional problem, aimed at easy adaptation of existing simulation tools. We give numerical examples that show the failure of existing formulations when applied to anisotropic faulted porous media, and go on to show the convergence of our method in both two-dimensional and three-dimensional.

KEYWORDS

discretization, faults, flow, mixed-dimensional, permeability, porous media

1 | INTRODUCTION

Modeling and simulation of flow in porous media with faults, fractures, and other thin inclusions representing discontinuities is central to a wide range of subsurface engineering applications, including geothermal energy exploitation,[1] shale gas extraction,[2] carbon sequestration,[3] and energy storage.[4]

The inclusions are characterized by a high aspect ratio, and permeability significantly different from that of the host medium; hence, they severely affect flow patterns. This poses a challenge for traditional simulation models, which are based on upscaling of fine-scale details into an equivalent permeability.[5-8] We instead focus on an alternative approach, which explicitly represents the inclusions in the mathematical and simulation models and thereby to a large degree avoids challenges related to parameter upscaling. To avoid elongated cells at the inclusion in the computational grid, it is common to represent the inclusions as codimension one objects embedded in the host medium.[9-12] The intersection of inclusions further gives rise to line and point intersections of codimension two and three. There are two ways of treating the

intersections. The first approach consists in representing explicitly the inclusions and host medium only, and making use of ad hoc conditions for the intersections, see, for example, References 13-16. We instead refer here to a second approach which has recently emerged (see, e.g., References 10,11,17), which consists in explicitly representing the intersections in the geometry. Following this approach, all objects (matrix, inclusions, and intersection points and lines) are equally represented in the model as independent subdomains separated by interfaces, and discretization models arise naturally, thereby avoiding challenges related to complex flow dynamics in the proximity of the intersections, for example, due to capillary flow or fractures with different permeabilities. We refer to this representation of the geometry as mixed-dimensional.

Governing equations for fluid flow in lower-dimensional representation of the inclusion can be derived by integration in the direction orthogonal to the inclusion. This leads to a decomposition of the governing equations into an in-plane component that represents flow within the inclusion, and an out-of-plane component that couples flow between the inclusion and the host medium. While the in-plane flow has been modeled with both linear[9,18-20] and nonlinear,[21-23] as well as with both isotropic and nonisotropic flow models, existing models for the coupling term are limited by an assumption on orthogonal flow between inclusion and host. Reduced-order models for flow were also developed for aquifers, leading to the same set of equations, see, for instance, References 24,25, and 26. The accuracy of the reduced models as compared with the full equi-dimensional model has been analyzed by several authors. Březina and Stebel[27] derived error estimates for the weak solution of the reduced model in comparison to the weak solution of the full model for anisotropic Darcy flow. Independently of the current article, Gander et al.[12] recently used a combination of Fourier analysis, asymptotic expansions, and functional analysis to obtain error estimates for the reduced models of anistropic diffusion in terms of the fracture width. However, both these studies treat the case of a domain containing a single fracture. A theoretical or numerical analysis of the case of a general network of fractures is still missing. For analysis of two-phase flow reduced models we refer the reader to References 23,25,28 and specifically to Reference 29 for Richards' equation. These existing models will be denoted as "local" in the following, meaning that the constitutive laws are local in both space and geometrical representation, the latter implying that the flux on any given subdomain (or boundary) is proportional to pressure gradients (or jumps) on the same subdomain.

Local models generally work well when the inclusion is a joint (tensile fracture). However, inclusions with a more complex geological history may have significantly more complex flow properties in the out-of-plane direction. For instance, the damage zone in the vicinity of faults may exhibit shear fractures, slip surfaces, and/or deformation bands, as summarized in Fossen et al.[30] These features introduce secondary permeability anisotropy in the damage zone as they tend to have preferred orientations, as shown by both field studies[31,32] and core analysis.[33] This leads to preferential flow directions that are neither parallel nor orthogonal to the main plane. This type of flow cannot be represented by existing simulation models that employ dimension reduction. To the Authors' best knowledge, the only attempt to simulating faults and their surrounding damage zones in a mixed-dimensional framework can be found in Reference 34. However, they still apply local formulations to model the damage zones as lower-dimensional objects which are connected on one side to the fault and on the other side to the rock matrix, hence conceptually seeing the whole fault zone as a multilayer object. An alternative approach would be to implement the fault core as a transmissibility multiplier and the damage zone by modifying the grid permeability in the cells adjacent to the model faults, as illustrated in Wilson et al.[35] In the following, we will consistently refer to the thin inclusions as faults, notwithstanding that all methods presented herein can be applied to models of fractures and other thin inclusions, however, we expect that the methods proposed are of more importance for faults.

The contribution of this article is twofold: First, we present a generalized dimensional reduced model that can preserve full-tensor permeability effects also in the out-of-plane direction of the fault. This type of mixed-dimensional problem involving general permeability tensors has only been treated in a recent publication by Gander et al.,[12] who used Fourier analysis to derive coupling conditions between a single fracture and the surrounding rock in a two-dimensional (2D) setting. It is interesting to note that both derivations lead to the same results. Herein, we further generalize the model to the case with a general network of inclusions. The resulting reduced equations have a form similar to that of traditional models, however, the more general coupling structure leads to additional terms both in the in-plane and out-of-plane equations. These terms, as well as our whole novel formulation, will be denoted as "semi-local" in the following, emphasizing the fact that the constitutive laws contain quantities that, while physically in the same location, from a modeling perspective are not local in terms of the geometry. As an example, the flux in a fault depends on the pressure jump (associated with the boundary of the rock), and conversely, the flow from the rock into the fault depends on the gradient of pressure in the fault.

Multiple discretization schemes have been proposed for the local dimensionally reduced models, including methods based on finite volumes,[13,14,36] mixed finite elements,[9,10] virtual elements,[37] and mimetic methods.[38] A comparison study for all these discretizations of flow in fractured media can be found in Flemisch et al.[39] and[40] for 2D and three-dimensional

(3D) flow, respectively. However, the additional terms arising in our formulation bring the semilocal model outside the scope of previously proposed discretization methods.

The second contribution of the article is therefore the derivation of discretization schemes for semilocal models. We achieve this in two stages: First, based on the unified framework for discretization of mixed-dimensional problems with local interface laws presented in Nordbotten et al.,[11] we present conditions under which any standard discretization scheme for fixed-dimensional problems can be extended to mixed-dimensional problems with semilocal interface laws. Second, we present a concrete discretization approach based on finite volume methods. An important consequence of this development is that we find that despite the geometric nonlocality allowed by the semilocal constitutive laws, the resulting numerical implementation retains the complexity of the discretization of local constitutive laws.

The article is organized as follows. In Section 2, the mathematical model is presented, first for a domain with a single fault, and then for a general faults configuration. Thereafter, in Section 3, the unified discretization is formulated. After presenting simulation results in Section 4, concluding remarks are given in Section 5.

2 | FLOW MODELLING IN FAULTED POROUS MEDIA

In this section, the mathematical model for flow in faulted porous media is presented, first for a porous domain containing a single fault (Sections 2.1 and 2.2), and then for a general network of faults (Section 2.3). For the general case, we also provide the weak formulation of the interface problem (Sections 2.4 and 2.5), which will be useful from the perspective of implementation. To this end, we remark that the derivations that follow are formal, in the sense that sufficient regularity is assumed for the equations to make sense. However, in order to accommodate the geometric complexities associated with faulted geometries, the equations should properly be understood in a weak sense, where the appropriate notions of continuous and weak spaces are defined in Reference 41.

2.1 | Domain with a single fault

We start by considering two 3D porous media Ψ_1 and Ψ_2, each of them with its Neumann and Dirichlet boundaries ∂_N and ∂_D, respectively. The two 3D domains are separated by a fault Ψ_3, which is a thin, almost 2D object of thickness a (in the following a will be denoted as the aperture), but which is currently represented as 3D. We note that Ψ_3 need not be planar, that is, a need not be constant. We denote by $\partial_{\Psi_3}\Psi_j$, for $j=1,2$, the boundary of Ψ_j adjacent to Ψ_3. Furthermore, let $\boldsymbol{n}_i$ be the normal vector which is always pointing outwards of Ψ_i. It thus follows that $\boldsymbol{n}_3 = -\boldsymbol{n}_j$ on $\partial_{\Psi_3}\Psi_j$. A representation of the fault as a thin 3D domain Ψ_3 is illustrated in the left of Figure 1. Darcy flow in the 3D porous medium is then governed by the following set of equations ($i=1,2,3$):

$$\nabla \cdot \boldsymbol{q}_i + f_i = 0 \qquad \text{on} \quad \Psi_i \tag{1}$$

$$\boldsymbol{q}_i = -\boldsymbol{K}_i \nabla p_i \qquad \text{on} \quad \Psi_i \tag{2}$$

$$\lambda_{3,j} = \boldsymbol{q}_3 \cdot \boldsymbol{n}_3 = -\boldsymbol{q}_j \cdot \boldsymbol{n}_j = -\lambda_{j,3} \qquad (j=1,2) \qquad \text{on} \quad \partial_{\Psi_3}\Psi_j \tag{3}$$

$$\boldsymbol{q}_i \cdot \boldsymbol{n}_i = g_i \qquad \text{on} \quad \partial_N \Psi_i \tag{4}$$

$$\text{tr}\ p_i = 0 \qquad \text{on} \quad \partial_D \Psi_i \tag{5}$$

Here, p is pressure, $\mathbf{q}$ is the Darcy flux, f is a source, and $\boldsymbol{K}$ is a second-order tensor representing the absolute permeability divided by fluid viscosity. Equation (1) represents mass conservation, while Equation (2) is Darcy's law. Equation (3) represents flux continuity conditions on $\partial_{\Psi_3}\Psi_j$, where $\lambda_{3,j}$ represents flow from Ψ_3 to Ψ_j, thus by flux continuity it follows that $\lambda_{3,j} = -\lambda_{j,3}$. Finally, Equations (4) and (5) are boundary conditions on $\partial_N\Psi_i$ and $\partial_D\Psi_i$, respectively.

Before deriving the governing equations for the lower-dimensional manifold, we discuss the decomposition of the permeability tensor within the fault. Existing local laws for faults as embedded thin inclusions assume that the principal directions of the local permeability tensor are aligned with the fault orientation, as shown in Figure 2(A). Hence, more general orientations of the permeability principal directions, shown in Figure 2(B,C), cannot be represented by existing models. To be concrete, we let the permeability on Ψ_3 have the following decomposition in terms of a coordinate system

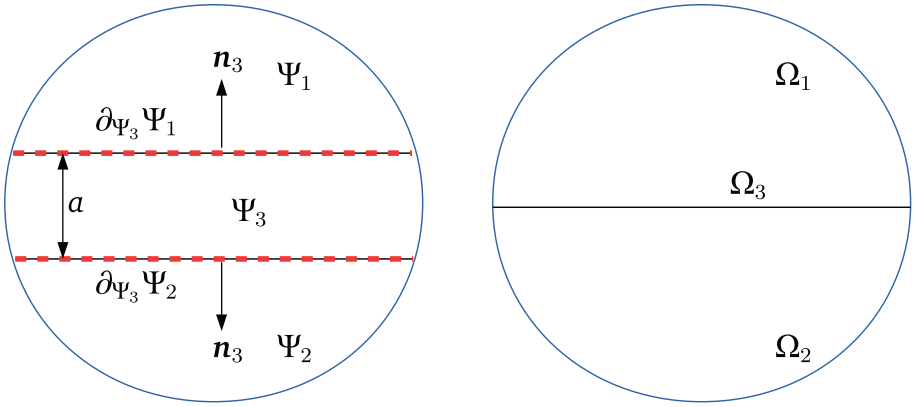

FIGURE 1 Representation of the fault as a thin three-dimensional domain Ψ_3 (left) and as a two-dimensional manifold Ω_3 (right). The boundary of Ψ_j adjacent to Ψ_3 is denoted by $\partial_{\Psi_3}\Psi_j$, for $j = 1, 2$, while $\boldsymbol{n}_i$ is the normal vector which is always pointing outwards from Ψ_i, for $i = 1, 2, 3$

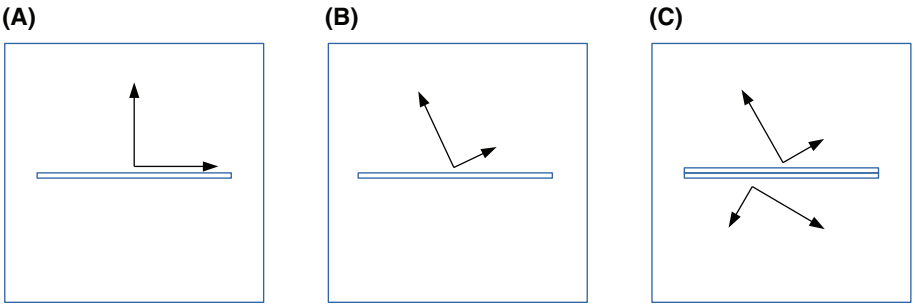

FIGURE 2 Illustration of possible structures of the permeability of a fault embedded in a porous domain indicated by the principal axis of the permeability tensor: (A) Orthogonal permeability, (B) homogeneous full-permeability structure, (C) different structure on each half of the fault

aligned with the fault orientation:

$$\boldsymbol{K}_3 = \begin{bmatrix} \boldsymbol{K}_{3,\parallel} & \boldsymbol{k}_{3,t} \\ \boldsymbol{k}_{3,t}^T & k_{3,\perp} \end{bmatrix} \tag{6}$$

Here, $\boldsymbol{K}_{3,\parallel}$ is a 2×2 second-order tensor representing the within-fault permeability and $k_{3,\perp}$ is a scalar representing the normal permeability. The off-diagonal term $\boldsymbol{k}_{3,t}$ is a two-vector representing the symmetric off-diagonal components of $\boldsymbol{K}_3$; for local interface laws, these off-diagonal components are assumed to be negligible, that is, $\boldsymbol{k}_{3,t} = 0$.[26,40] On the contrary, when $\boldsymbol{k}_{3,t} \neq 0$, the inclusion of this anisotropic term leads to significant complications in the modeling and discretization, and is the main topic of this work. With this structure of the fault permeability, the Darcy flux for the fault can be decomposed as $\boldsymbol{q}_3 = [\boldsymbol{q}_{3,\parallel}, q_{3,\perp}]$, where the two-vector tangential component $\boldsymbol{q}_{3,\parallel}$ and the scalar normal component $q_{3,\perp}$ have the following form:

$$\boldsymbol{q}_{3,\parallel} = -\boldsymbol{K}_{3,\parallel}\nabla_{\parallel} p_3 - \boldsymbol{k}_{3,t}\nabla_{\perp} p_3, \tag{7}$$

$$q_{3,\perp} = -\boldsymbol{k}_{3,t}\cdot\nabla_{\parallel} p_3 - k_{3,\perp}\nabla_{\perp} p_3. \tag{8}$$

Here, $\nabla_{\parallel}$ and $\nabla_{\perp} = \frac{\partial}{\partial n}$ represent the in-plane and out-of-plane components of the gradient for the fault, respectively.

2.2 | Model reduction

To proceed, we apply integration over the perpendicular direction to achieve a dimension reduction of the fault. This replaces Ψ_3 with a lower-dimensional domain Ω_3 (see right of Figure 1). Note that we use Ψ to represent the equi-dimensional geometry, that is all Ψ_j are 3D, and Ω to denote the mixed-dimensional geometry. We also introduce two interfaces $\Gamma_{j,3}$ on each side $j = 1, 2$ of Ω_3, as shown in Figure 3. The interfaces physically represent the half zone comprised between the fault and either side of the surrounding matrix. In a mixed-dimensional setting, they have no perpendicular extent, and serve as connectors between two objects of different dimensions. Note that, due to the dimension reduction of the model, Ω_3, $\Gamma_{1,3}$, $\Gamma_{2,3}$, $\partial_{\Omega_3}\Omega_1$, and $\partial_{\Omega_3}\Omega_2$ are all coinciding in physical space. Furthermore, we define the integrated

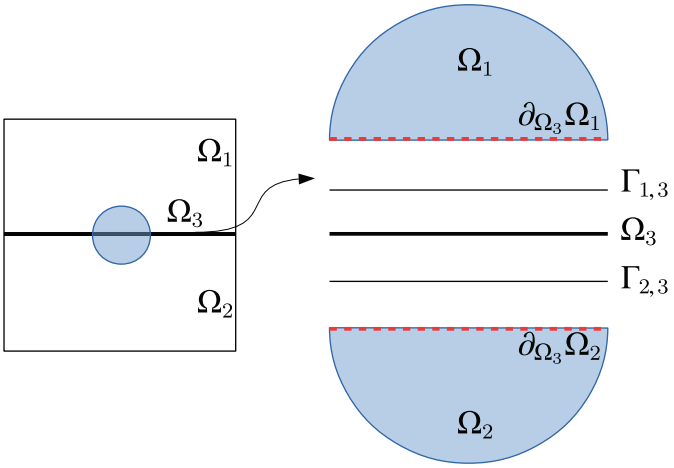

FIGURE 3 Illustration of the mixed-dimensional geometry. Ω_3 is connected to the higher-dimensional neighbors Ω_j through the interfaces $\Gamma_{j,3}$, for $j = 1, 2$. Note that Ω_3, $\Gamma_{j,3}$, and $\partial_{\Omega_3}\Omega_j$ are all coinciding in physical space

Darcy flux $\boldsymbol{q}_3^{(2)}$ and the average pressure $p_3^{(2)}$, respectively as

$$\boldsymbol{q}_3^{(2)} = \int_{-a/2}^{a/2} \boldsymbol{q}_{3,\parallel}^{(3)} dn, \qquad p_3^{(2)} = \frac{1}{a}\int_{-a/2}^{a/2} p_3^{(3)} dn. \tag{9}$$

Here, we use subscripts to index the domains, and superscripts (when necessary for clarity) to emphasize the effective topological dimension of the domain, for example, $p_3^{(3)}$ and $p_3^{(2)}$ are the pressures within the fault in the 3D (on Ψ_3) and 2D (on Ω_3) representations, respectively. When passing to a mixed-dimensional representation of the geometry, that is, when integrating Equations (1) and (7) along the perpendicular direction, the out-of-plane component of the gradient is converted into a jump operator as follows:

$$\int_{-a/2}^{a/2} \nabla_\perp p_3^{(3)} dn = (\text{tr } p_1 - \text{tr } p_2). \tag{10}$$

The governing equations for the fault are then obtained from Equations (1), (7), (4), and (5) by integrating in the perpendicular direction. Moreover, since the fault is assumed to be thin, we let the permeability be constant across the perpendicular direction on each side of the fault. Together with the definitions above, this results in

$$\nabla_3 \cdot \boldsymbol{q}_3^{(2)} - (\lambda_{1,3} + \lambda_{2,3}) + f_3^{(2)} = 0 \quad \text{on} \quad \Omega_3 \tag{11}$$

$$\boldsymbol{q}_3^{(2)} = -a\boldsymbol{K}_{3,\parallel}\nabla_3 p_3^{(2)} + \boldsymbol{\mu}_{1,3} + \boldsymbol{\mu}_{2,3} \quad \text{on} \quad \Omega_3 \tag{12}$$

$$\boldsymbol{q}_3^{(2)} \cdot \boldsymbol{n}_3^{(2)} = g_3^{(2)} \quad \text{on} \quad \partial_N\Omega_3 \tag{13}$$

$$\text{tr } p_3^{(2)} = 0 \quad \text{on} \quad \partial_D\Omega_3 \tag{14}$$

where we have also introduced the integrated source term and boundary flux

$$f_3^{(2)} = \int_{-a/2}^{a/2} f_3^{(3)} dn, \qquad g_3^{(2)} = \int_{-a/2}^{a/2} g_3^{(3)} dn. \tag{15}$$

We emphasize that the differential operator ∇_3 in Equations (11) and (12) operates on the manifold Ω_3. Compared with traditional upscaled models, see, for instance, Nordbotten et al.,[11] additional terms $\boldsymbol{\mu}_{j,3}$ appear in Equation (12), analogous to the flux terms $\lambda_{j,3}$ in Equation (11). This two-vector term, which is not present in previous work, represents the within-fault flux induced by pressure differences between the fault and the surrounding matrix, and is defined for either side of the fault as

$$\boldsymbol{\mu}_{j,3} = \epsilon_{j,3}\boldsymbol{k}_{3,j,t}(p_3^{(2)} - \text{tr } p_j), \tag{16}$$

where the permutation variable $\epsilon_{j,3}$ is positive if the coordinate systems of Ω_3 and $\partial_{\Omega_3}\Omega_j$ coincide, and negative otherwise. The presence of the trace operator in Equation (16) explains why we termed our formulation "semi-local," that is we emphasize that material laws which are local in space are nonlocal with respect to the geometric representation. This can be easily seen when substituting Equation (16) into Equation (12), one obtains a flux which, while defined on Ω_3, from a modeling perspective contains quantities residing outside Ω_3, specifically tr p_j.

To complete the model, we derive a constitutive law for $\lambda_{j,3}$. This is obtained by integrating Equation (8) in the perpendicular direction, that is

$$\int_{-a/2}^{a/2} q_{3,\perp}^{(3)} dn = -\int_{-a/2}^{a/2} \boldsymbol{k}_{3,t} \cdot \nabla_{\parallel} p_3^{(3)} dn - \int_{-a/2}^{a/2} k_{3,\perp} \nabla_{\perp} p_3^{(3)} dn. \tag{17}$$

The left-hand side of Equation (17) is approximated using the trapezoidal rule, that is

$$\int_{-a/2}^{a/2} q_{3,\perp}^{(3)} dn \approx \frac{a}{2}(\epsilon_{1,3}\lambda_{1,3} + \epsilon_{2,3}\lambda_{2,3}), \tag{18}$$

where continuity of the flux across the boundary between the fault and the surrounding matrix is applied. The first term at the right-hand side of Equation (17) is approximated as

$$\begin{aligned}\int_{-a/2}^{a/2} \boldsymbol{k}_{3,t} \cdot \nabla_{\parallel} p_3^{(3)} dn &= \boldsymbol{k}_{3,2,t} \cdot \int_{-a/2}^{0} \nabla_{\parallel} p_3^{(3)} dn + \boldsymbol{k}_{3,1,t} \cdot \int_{0}^{a/2} \nabla_{\parallel} p_3^{(3)} dn \\ &\approx \frac{a}{2}\left(\boldsymbol{k}_{3,1,t} + \boldsymbol{k}_{3,2,t}\right) \cdot \nabla_3 p_3^{(2)}.\end{aligned} \tag{19}$$

Finally, the second term at the right-hand side of (17) is resolved using the jump operator defined in Equation (10) as follows:

$$\int_{-a/2}^{a/2} k_{3,\perp} \nabla_{\perp} p_3^{(3)} dn = \epsilon_{1,3} k_{3,1,\perp}(p_3^{(2)} - \text{tr } p_1) + \epsilon_{2,3} k_{3,2,\perp}(p_3^{(2)} - \text{tr } p_2). \tag{20}$$

By incorporating Equations (18)–(20) into Equation (17), we identify the flux $\lambda_{j,3}$ having the following form:

$$\lambda_{j,3} = -k_{3,j,\perp} \frac{2(p_3^{(2)} - \text{tr } p_j)}{a} - \epsilon_{j,3} \boldsymbol{k}_{3,j,t} \cdot \nabla_3 p_3^{(2)}. \tag{21}$$

Here, the first term on the right-hand side represents the local component of the constitutive law, while the second part is the semilocal contribution that induces a flux across $\Gamma_{j,3}$ due to the pressure gradient within the lower-dimensional manifold Ω_3. Inspecting Equations (16) and (21), we see that both the normal permeability $k_{3,j,\perp}$ and the off-diagonal permeability $\boldsymbol{k}_{3,j,t}$ are in the reduced model naturally interpreted as properties of the interface $\Gamma_{j,3}$. In the continuation, we will thus assign these quantities independently to each side of the fault. It is interesting to see that, upon incorporation of Equation (16) into Equation (12), substituting Equation (12) into (11) and taking the sum of the two sides of Equation (21), one obtains the same coupling conditions derived in Gander et al.[12]

In summary, omitting superscripts for the sake of clarity, we can write the mixed-dimensional Equations (1)–(5), (11)–(14), (16), and (21) in a unified way, that is for $i \in \{1, 2, 3\}$

$$\nabla_i \cdot \boldsymbol{q}_i - \sum_{j \in \hat{S}_i} \lambda_{j,i} + f_i = 0 \qquad \text{on} \quad \Omega_i \tag{22}$$

$$\boldsymbol{q}_i = -\boldsymbol{\kappa}_{i,\parallel} \nabla_i p_i + \sum_{j \in \hat{S}_i} \epsilon_{j,i} \boldsymbol{\kappa}_{i,j,t}(p_i - \text{tr } p_j) \qquad \text{on} \quad \Omega_i \tag{23}$$

$$\boldsymbol{q}_i \cdot \boldsymbol{n}_i = \lambda_{i,3} \qquad (i \neq 3) \qquad \text{on} \quad \partial_{\Omega_3}\Omega_i \tag{24}$$

$$\lambda_{j,3} = -\kappa_{3,j,\perp}(p_3 - \text{tr } p_j) - \boldsymbol{\kappa}_{3,j,t} \cdot \nabla_3 p_3 \qquad (j = 1, 2) \qquad \text{on} \quad \Gamma_{j,3} \tag{25}$$

$$\boldsymbol{q}_i \cdot \boldsymbol{n}_i = g_i \qquad \text{on} \quad \partial_N \Omega_i \tag{26}$$

$$\text{tr } p_i = 0 \qquad \text{on} \quad \partial_D \Omega_i \tag{27}$$

where $\hat{S}_i$ is the set of neighbors of Ω_i of higher dimension, for example, $\hat{S}_3 = \{\Omega_1, \Omega_2\}$. Equations (22)–(27) are complemented with the natural convention that there is no four-dimensional domain in the model, thus $\hat{S}_i = \emptyset$ for $i = 1, 2$, and one clearly has for these 3D domains also that $a = 1$, $\boldsymbol{K}_{\|} = \boldsymbol{K}$, and $\nabla_i = \nabla$.

We remark that due to the model reduction, the within-fault permeability $\boldsymbol{K}_{3,\|}$ and the normal permeability $k_{3,j,\perp}$ scale with the aperture a and its inverse, respectively, while the off-diagonal permeability $\boldsymbol{k}_{3,j,t}$ remains as in the equi-dimensional model. In order to present Equations (22)–(27) without reference to this small parameter, these scalings have been incorporated directly into the material constants. Thus, the mixed-dimensional permeability $\boldsymbol{\kappa}_3$ is related to the equi-dimensional $\boldsymbol{K}_3$ as follows

$$\boldsymbol{\kappa}_3 = \begin{bmatrix} \boldsymbol{\kappa}_{3,\|} & \boldsymbol{\kappa}_{3,j,t} \\ \boldsymbol{\kappa}_{3,j,t}^T & \kappa_{3,j,\perp} \end{bmatrix} = \begin{bmatrix} a\boldsymbol{K}_{3,\|} & \boldsymbol{k}_{3,j,t} \\ \boldsymbol{k}_{3,j,t}^T & 2a^{-1}k_{3,j,\perp} \end{bmatrix}. \tag{28}$$

We point out that, when one reduces multiple dimensions at once, these scalings get exponents corresponding to the number of dimensions below the ambient dimension. We also emphasize that the normal and off-diagonal permeabilities are in principle not a property of the fault itself, but instead a property which belongs to the internal interface $\Gamma_{j,3}$ between the fault and either side of the higher-dimensional neighbors. This represents an important extension of the existing local laws for fractured porous media, making the model also applicable to faulted porous media, since it allows for capturing the anisotropic character of the fault damage zone. Moreover, since different values of $\boldsymbol{k}_{3,j,t}$ and $k_{3,j,\perp}$ can be assigned to each side of the fault, our model can represent different permeability structures on each side of the fault.

A schematic illustration of the different quantities and their domain of definition for the local and semilocal formulations is shown in Figure 4.

2.3 | Domain with a general network of faults

Following the formulation by Boon et al.,[10] Equations (22)–(27) can be generalized also to faults intersections, both the one-dimensional (1D) line intersections between two faults and the zero-dimensional point intersections of three faults (see Figure 5 for an illustration of the mixed-dimensional geometry). To this end, we use subscripts to index each domain (matrix, fault, or intersection) by number as in the previous section, and let I denote the index set of all domains. Superscripts for the topological dimension associated with each individual domain will be consistently omitted, keeping in mind that the dimension is always a property of the domain, that is, $d = d_i$. Hence, we can write for all $i \in I$ the equations

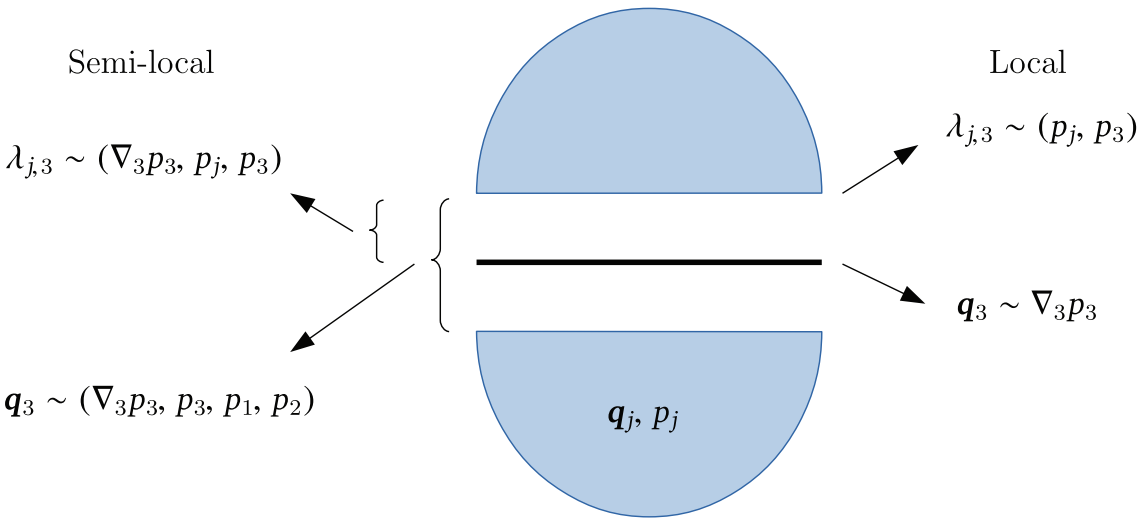

FIGURE 4 Illustration of the quantities associated with the local and semilocal formulations

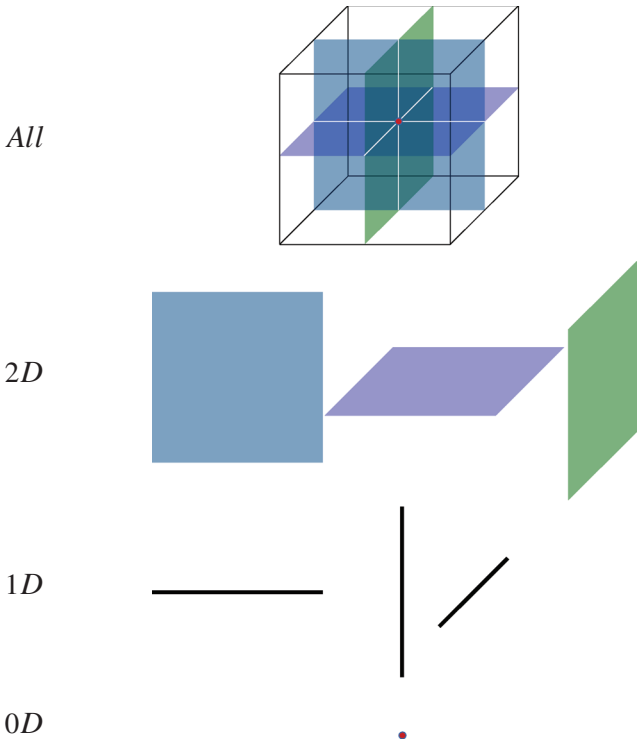

FIGURE 5 Illustration of the decomposition of a three-dimensional domain containing a network of three faults. From top to bottom: All mixed-dimensional domains, the three faults, the three one-dimensional fault intersections, and the zero-dimensional point intersection

$$\nabla_i \cdot \boldsymbol{q}_i - \sum_{j \in \hat{S}_i} \lambda_{j,i} + f_i = 0 \qquad \text{on} \quad \Omega_i \tag{29}$$

$$\boldsymbol{q}_i = -\boldsymbol{\kappa}_{i,\parallel} \nabla_i p_i + \sum_{j \in \hat{S}_i} \epsilon_{j,i} \boldsymbol{\kappa}_{i,j,t} (p_i - \text{tr } p_j) \qquad \text{on} \quad \Omega_i \tag{30}$$

$$\boldsymbol{q}_i \cdot \boldsymbol{n}_i = \lambda_{i,j} \qquad (j \in \check{S}_i) \qquad \text{on} \quad \partial_{\Omega_j} \Omega_i \tag{31}$$

$$\lambda_{j,i} = -\kappa_{i,j,\perp} (p_i - \text{tr } p_j) - \epsilon_{j,i} \boldsymbol{\kappa}_{i,j,t} \cdot \nabla_i p_i \qquad (j \in \hat{S}_i) \qquad \text{on} \quad \Gamma_{j,i} \tag{32}$$

$$\boldsymbol{q}_i \cdot \boldsymbol{n}_i = g_i \qquad \text{on} \quad \partial_N \Omega_i \tag{33}$$

$$\text{tr } p_i = 0 \qquad \text{on} \quad \partial_D \Omega_i \tag{34}$$

where $\check{S}_i$ is the set of neighbors of Ω_i of lower dimension, for example, $\check{S}_1 = \{\Omega_2, \Omega_3, \Omega_4\}$.

2.4 | Mixed-dimensional formulation of the fault-matrix flows

While Equations (29)–(34) constitute a full semilocal model, they are stated in a form which is not immediately amenable for discretization. This and the following subsection explore the model in more detail, with a goal of rewriting the equations in a form that can be handled by standard discretization schemes with only minimal adaptations. A discretization approach based on this reformulation is then given in Section 3.

In order to simplify the exposition, we will introduce a mixed-dimensional notation following Nordbotten et al.[11] In particular, we will denote the collection of pressure functions as $\mathfrak{p} = (p_1, \dots, p_{|I|})$, and similarly the collection of all fluxes (both in domains and across boundaries) as $\mathfrak{q} = (\boldsymbol{q}_1, \dots, \boldsymbol{q}_{|I|}, \lambda_{1,1}, \dots, \lambda_{|I|,|J|})$. It is sometimes convenient to refer explicitly to only the domain or boundary fluxes, and we will therefore sometimes abuse notation and simply write $\mathfrak{q} = (q, \lambda)$. We refer to these as mixed-dimensional functions, and consistently denote them with calligraphic font. We adopt the natural convention that when evaluating a mixed-dimensional function at a point, say $x \in \Omega_i$, then we simply evaluate the function on that domain, so that $\mathfrak{p}(x) = p_i(x)$. In a similar sense, we denote the disjoint union of domains as $\mathfrak{F} = \left(\coprod_i \Omega_i\right) \sqcup \left(\coprod_{j,i} \Gamma_{j,i}\right)$.

With this notion of mixed-dimensional functions, the extension of the divergence and gradient operators to the mixed-dimensional setting is natural. First, we extend the concept of continuous functions by requiring that for $\mathfrak{q}$ to be continuous, then it must hold that, for all $\Gamma_{j,i}$, $\boldsymbol{q}_i \cdot \boldsymbol{n}_i = \lambda_{i,j}$. Then, for any point $x \in \Omega_i$ we define

$$(\mathfrak{D} \cdot \mathfrak{q})(x) = \left[\nabla_i \cdot \boldsymbol{q}_i - \sum_{j \in \hat{S}_i} \lambda_{j,i} \right]_x \qquad \text{and} \qquad (\mathbb{D}\mathfrak{p})(x) = \left[\nabla_i p_i \right]_x, \tag{35}$$

while for any point on an interface $x \in \Gamma_{j,i}$ we define

$$(\mathbb{D}\mathfrak{p})(x) = \left[p_i - \operatorname{tr}\ p_j \right]_x. \tag{36}$$

Now we can write Equations (29)–(34) compactly as:

$$\mathfrak{D} \cdot \mathfrak{q} + \mathfrak{f} = 0 \qquad \text{on} \quad \mathfrak{F} \tag{37}$$

$$\mathfrak{q} = -\mathfrak{K}\mathbb{D}p \qquad \text{on} \quad \mathfrak{F} \tag{38}$$

$$\mathfrak{q} \cdot \mathfrak{n} = \mathfrak{g} \qquad \text{on} \quad \partial_N \mathfrak{F} \tag{39}$$

$$\operatorname{tr}\ \mathfrak{p} = 0 \qquad \text{on} \quad \partial_D \mathfrak{F} \tag{40}$$

where we have also introduced the collection of sources $\mathfrak{f} = \left(f_1, \ldots, f_{|I|}\right)$ and the collection of boundary fluxes $\mathfrak{g} = \left(g_1, \ldots, g_{|I|}\right)$. Here, the material coefficients are now all part of the mixed-dimensional permeability $\mathfrak{K}$, which is defined such as that for any mixed-dimensional gradient $\mathfrak{u} = \mathbb{D}p = (u, \mu)$, it holds that for any point $x \in \Omega_i$:

$$(\mathfrak{K}\mathfrak{u})(x) = \boldsymbol{\kappa}_{i,\parallel} u_i - \sum_{j \in \hat{S}_i} \epsilon_{j,i} \boldsymbol{\kappa}_{i,j,t} \mu_{j,i}, \tag{41}$$

while for any point on an interface $x \in \Gamma_{j,i}$, it holds that

$$(\mathfrak{K}\mathfrak{u})(x) = \kappa_{i,j,\perp} \mu_{j,i} + \epsilon_{j,i} \boldsymbol{\kappa}_{i,j,t} \cdot u_i. \tag{42}$$

It is then also sometimes convenient to write Equation (38) in matrix form, that is for $\mathfrak{q} = (q, \lambda)$ and $\mathfrak{u} = \mathbb{D}\mathfrak{p} = (u, \mu)$, one has:

$$\begin{Bmatrix} q \\ \lambda \end{Bmatrix} = - \begin{bmatrix} \mathfrak{K}_{\Omega\Omega} & \mathfrak{K}_{\Omega\Gamma} \\ \mathfrak{K}_{\Gamma\Omega} & \mathfrak{K}_{\Gamma\Gamma} \end{bmatrix} \begin{Bmatrix} u \\ \mu \end{Bmatrix}. \tag{43}$$

Equation (43) highlights the contribution from the semilocal terms in the mixed-dimensional version of Darcy's law, since, for local constitutive laws, the permeability is block diagonal when expressed in this way, with both $\mathfrak{K}_{\Gamma\Omega}$ and $\mathfrak{K}_{\Omega\Gamma}$ vanishing.

One can show that as long as the all in-plane permeabilites $\boldsymbol{\kappa}_{i,\parallel}$ are symmetric positive definite, and the mixed-dimensional permeabilities are diagonally dominant in the sense of satisfying

$$\kappa_{i,j,\perp} \det \boldsymbol{\kappa}_{i,\parallel} > \boldsymbol{\kappa}_{i,j,t} \cdot \boldsymbol{\kappa}_{i,j,t}, \tag{44}$$

then the coefficients are globally positive definite, and Equations (37)–(40) are well-posed with a unique weak solution, as long as $\partial_D \Omega_i$ has nonzero measure for at least one domain. This can be proven using the functional analysis tools for mixed-dimensional problems described in Boon et al.[41] In particular, our stated conditions ensure that the mixed-dimensional coefficients are symmetric positive definite as defined in Boon et al.,[41] thus their theorems 4.1 and 4.2 apply, and problem (37)–(40) are the Euler–Lagrange equations of a coercive minimization problem, which has a unique minimum in the appropriately defined Hilbert spaces.

2.5 | Weak formulation as an interface system

The semilocal terms in Equations (29)–(34) lead to coupling terms between domains that are local in physical space, but nonlocal in the mixed-dimensional representation of the geometry. A critical example are the fault and its sides, which, from the perspective of implementation, we would prefer to only interact via the interfaces $\Gamma_{j,i}$, and not directly, as is the case for the last term in Equation (30).

Thus, we are motivated to consider a reformulation of the governing equations before considering numerical discretizations. To this end, we recall that the model equations are to be understood weakly, and that it is therefore both desirable to express the coupling conditions weakly in order to ensure a good numerical method. We proceed by first performing an LU decomposition of Equation (43) as follows:

$$\mathfrak{K}_U \begin{Bmatrix} q \\ \lambda \end{Bmatrix} = -\mathfrak{K}_L \begin{Bmatrix} u \\ \mu \end{Bmatrix}, \tag{45}$$

where $\mathfrak{K}_U$ and $\mathfrak{K}_L$ are defined, respectively as:

$$\mathfrak{K}_U = \begin{bmatrix} I & \mathfrak{K}_{\Omega\Gamma}\mathfrak{K}_{\Gamma\Gamma}^{-1} \\ 0 & I \end{bmatrix} \qquad \text{and} \qquad \mathfrak{K}_L = \begin{bmatrix} A_\Omega & 0 \\ \mathfrak{K}_{\Gamma\Omega} & \mathfrak{K}_{\Gamma\Gamma} \end{bmatrix}, \tag{46}$$

and A_Ω is the Schur-complement defined as

$$A_\Omega = \mathfrak{K}_{\Omega\Omega} - \mathfrak{K}_{\Omega\Gamma}\mathfrak{K}_{\Gamma\Gamma}^{-1}\mathfrak{K}_{\Gamma\Omega}. \tag{47}$$

Note that, since $\mathfrak{K}_{\Gamma\Gamma}$ consists only of scalar values ($\kappa_{i,j,\perp}$), this reformulation only depends on the trivial inversion of scalars.

In the following it will be helpful to discuss the components of the mixed-dimensional gradient and divergence, and we therefore additionally define the "full jump" $\mathbb{d}\mathfrak{q}$ such that for any point $x \in \Omega_i$ it holds that

$$(\mathbb{d}\mathfrak{q})(x) = \left[-\sum_{j \in \hat{S}_i} \lambda_{j,i} \right]_x, \tag{48}$$

while the "half jump" $\mathbb{d}^\star\mathfrak{p}$ is simply the restriction of $\mathbb{D}\mathfrak{p}$ to $\Gamma_{j,i}$. We then write (with the natural extension of ∇ and $\nabla\cdot$):

$$\mathfrak{D}\cdot\mathfrak{q} = \nabla\cdot q + \mathbb{d}\lambda \qquad \text{and} \qquad \mathbb{D}\mathfrak{p} = \left(\nabla p, \mathbb{d}^\star\mathfrak{p}\right). \tag{49}$$

We now proceed by (formally) eliminating internal domain variables, in order to obtain a problem only posed on interfaces. We note that Equations (37) and (38) can now be written as the first-order system:

$$\mathfrak{D}\cdot\mathfrak{q} = \mathfrak{f} \tag{50}$$
$$\mathfrak{K}_U\mathfrak{q} = -\mathfrak{K}_L\mathfrak{D}\mathfrak{p} \tag{51}$$

where use of Equation (45) has been made. By writing out Equation (50) in local notation for each Ω_i and by stating Equation (51) explicitly as two equations, we obtain the following set of equations:

$$\nabla\cdot q = f - \mathbb{d}\lambda \tag{52}$$
$$q + A_\Omega\nabla p = -\mathfrak{K}_{\Omega\Gamma}\mathfrak{K}_{\Gamma\Gamma}^{-1}\lambda \tag{53}$$
$$\lambda = -\left(\mathfrak{K}_{\Gamma\Omega}\nabla p + \mathfrak{K}_{\Gamma\Gamma}\mathbb{d}^\star\mathfrak{p}\right) \tag{54}$$

This reveals that Equations (52) and (53) form a locally well-posed system (of standard Darcy type) on each Ω_i, and we can therefore consider $p = p(\lambda)$ for any given λ.

We formalize this concept by introducing the (continuous) solution operators for the standard elliptic value problem on Ω_i, $\mathcal{S}^K_{\Omega_i}$, defined as:

$$(v, \nabla v, \mathrm{tr}\ \ v, F) = \mathcal{S}^K_{\Omega_i}(f, \chi, b, v_0), \tag{55}$$

where v is the solution to

$$\nabla \cdot \varphi = f - F \quad \text{on} \quad \Omega_i \tag{56}$$
$$\varphi = -K(\nabla v + \chi) \quad \text{on} \quad \Omega_i \tag{57}$$
$$\varphi \cdot n = b \quad \text{on} \quad \partial\Omega_i \setminus \partial\Omega \tag{58}$$
$$v = 0 \quad \text{on} \quad \partial\Omega_i \cap \partial\Omega \tag{59}$$
$$\frac{1}{|\Omega_i|}\int_{\Omega_i} v = v_0 \quad \text{if} \quad \partial\Omega_i \cap \partial\Omega \neq \emptyset \tag{60}$$

where $\partial\Omega$ is the global boundary and $F = \frac{1}{|\Omega_i|}\left(\int_{\Omega_i} f - \int_{\Omega_i} b\right)$ if $\partial\Omega_i \cap \partial\Omega \neq \emptyset$, and zero otherwise. Using this solution operator, we see that the solution to Equations (52) and (53) can be stated as functions of λ (and a set of number of numbers p_0 corresponding to the domains where $\partial\Omega_i \cap \partial\Omega \neq \emptyset$) as:

$$(p, \nabla p, \mathrm{tr}\ \ p, F)_{\Omega_i}(\lambda, p_0) = \mathcal{S}^{A_i}_{\Omega_i}\left(f_i - (\mathbb{d}\lambda)_i, A_i^{-1}\left(\mathfrak{K}_{\Omega\Gamma}\mathfrak{K}^{-1}_{\Gamma\Gamma}\lambda\right)_i, \lambda_{\check{I}_i}, p_0\right). \tag{61}$$

Inserting $p = p(\lambda, p_0)$ and so forth into Equation (54), we have now reformulated the fault-matrix problem into a pure interface problem. From the perspective of implementation, we desire to consider the interface problem in the weak sense, and we therefore multiply by test functions w and integrate to obtain the problem: Find $\lambda \in L^2(\Gamma)$ such that, for all $w \in L^2(\Gamma_j)$

$$\left(\mathfrak{K}^{-1}_{\Gamma\Gamma}\lambda, w\right)_{\Gamma_{j,i}} + \left(\mathfrak{K}^{-1}_{\Gamma\Gamma}\mathfrak{K}_{\Gamma\Omega}\nabla p(\lambda, p_0), w\right)_{\Gamma_{j,i}} + \left(\mathbb{d}^\star \mathfrak{p}(\lambda, p_0), w\right)_{\Gamma_{j,i}} = 0 \tag{62}$$

and $F_i(\lambda, p_0) = 0$ if $\partial\Omega_i \cap \partial\Omega \neq \emptyset$. We point out that the inner products in Equation (62) are bounded from a formal perspective, since for $\lambda \in L^2(\Gamma)$, then $p_i \in H^1(\Omega_i)$, and both $\mathfrak{K}^{-1}_{\Gamma\Gamma}\mathfrak{K}_{\Gamma\Omega}\nabla p$ and tr p will lie in (at least) $L^2(\Gamma_{j,i})$.

Finally, we emphasize that Equations (61) and (62) are attractive from the perspective of implementation, since the inner products appearing are easy to evaluate, and the solution operators $\mathcal{S}^{A_i}_{\Omega_i}$ can be approximated by any standard numerical method, as we will detail in the following section.

3 | DISCRETIZATIONS OF FLOW FOR FAULTED POROUS MEDIA

The equations derived in Section 2.5, and in particular the interface problem of Equation (61), form the starting point for the discretization approach laid out in this section. We present the general discretization framework in Section 3.1, and discuss implementational aspects in Section 3.2.

3.1 | Unified discretization

Equation (61) provides a solution operator for the arbitrary standard method used to solve the elliptic boundary value problem (52) and (53) on Ω_i. To be concrete, we consider each domain Ω_i and its Neumann boundary $\partial\Omega_i = \partial_N\Omega_i \cup \sum_{j\in\check{S}_i}\partial_{\Omega_j}\Omega_i$ as endowed with a numerical discretization. Then, the solution operator $\mathcal{S}_i$ can be stated as

$$\mathcal{S}_i : \left[N(\Omega_i), N^{d_i}(\Omega_i), N(\partial\Omega_i)\right] \to \left[N(\Omega_i), N^{d_i}(\Omega_i), N(\partial\Omega_i)\right], \tag{63}$$

where $N(\Omega_i)$, $N^{d_i}(\Omega_i)$, and $N(\partial\Omega_i)$ are the discrete representations of $L^2(\Omega_i)$, $\left(L^2(\Omega_i)\right)^{d_i}$, and $L^2(\partial\Omega_i)$, respectively, and d_i is the topological dimension of Ω_i. In particular, $\mathcal{S}_i$ takes as input sinks, vector sources, and Neumann data and returns as output pressures, pressure gradients, and pressure traces. Most discretization schemes for elliptic equations can provide such a solution operator; we discuss the concrete implementation in the following subsection.

To discretize the flux coupling term $\lambda_{j,i}$, we introduce a mortar-like grid $\mathcal{T}_{j,i}$ on the interface $\Gamma_{j,i}$ on which the boundary flux $\lambda_{j,i}$ will be defined. The flux variables are represented as piecewise constant on the mortar grid $\mathcal{T}_{j,i}$, thus $\lambda_{j,i} \in P_0(\mathcal{T}_{j,i}) \subset Ł^2(\Omega_i)$. In order to allow communications between subdomains, and thus explicitly relate the degrees of freedom of the numerical methods $\mathcal{S}_i$ and the mortar grids $\mathcal{T}_{j,i}$, we introduce projection operators, namely, $\Pi_{N(\Omega_i)}$ and $\Pi_{L^2(\Omega_i)}$. The former is the compound operator projecting from the coupling variables on the mortar grids to the subdomain degrees of freedom, that is

$$\begin{aligned}\Pi_{N(\Omega_i)} : &\left[L^2(\Omega_i), \left(L^2(\Omega_i)\right)^{d_i}, L^2\left(\Omega_{\check{S}_i}\right), L^2(\partial\Omega_i)\right] \\ &\rightarrow \left[N(\Omega_i), N^{d_i}(\Omega_i), N(\partial\Omega_i)\right],\end{aligned} \tag{64}$$

while the latter conversely moves from the numerical variables to the coupling variables, that is

$$\begin{aligned}\Pi_{L^2(\Omega_i)} : &\left[N(\Omega_i), N^{d_i}(\Omega_i), N(\partial\Omega_i)\right] \\ &\rightarrow \left[L^2(\Omega_i), \left(L^2(\Omega_i)\right)^{d_i}, L^2\left(\Omega_{\check{S}_i}\right), L^2(\partial\Omega_i)\right].\end{aligned} \tag{65}$$

Now, following the variational formulation derived in Section 2.5, we exploit Equation (62) in order to provide discretization-independent framework for faulted porous media. This takes the form: for given numerical discretizations $\mathcal{S}_i$, find $\lambda_{j,i} \in P_0(\mathcal{T}_{j,i})$, for all $i \in I$ and $j \in \hat{S}_i$ such that

$$\begin{aligned}&\left(\mathrm{d}^\star \mathfrak{p}, w_j\right)_{\Gamma_{j,i}} + \left(\mathfrak{K}_{\Gamma\Gamma}^{-1}\left(\lambda_{j,i} + \mathfrak{K}_{\Gamma\Omega} \cdot \nabla p\right), w_j\right)_{\Gamma_{j,i}} = 0 \\ &\quad \text{for all } \; w_j \in P_0(\mathcal{T}_{j,i})\end{aligned} \tag{66}$$

subject to discrete constraints (for all $i \in I$):

$$[p_i, u_i, t_j] = \Pi_{L^2(\Omega_i)} \mathcal{S}_i(\psi_i + a_i, b_i, c_i) \tag{67}$$

$$[a_i, b_i, c_i] = \Pi_{N(\Omega_i)} \left[-\sum_{j \in \hat{S}_i} \lambda_{j,i}, -\sum_{j \in \hat{S}_i} A_i^{-1} \mathfrak{K}_{\Omega\Gamma} \mathfrak{K}_{\Gamma\Gamma}^{-1} \lambda_{j,i}, \sum_{j \in \check{S}_i} \lambda_{i,j} \right] \tag{68}$$

where the dummy variables a_i, b_i, and c_i have the interpretations of sources, forces, and fluxes due to interactions with other domains, respectively. By contrast, the variables p_i, u_i, and t_j are the pressures, pressure gradients, and pressure traces after projection onto the grids $\mathcal{T}_{j,i}$.

The interpretation of this scheme is as follows. Equation (67) resolves the internal differential equations in each subdomain, Equation (68) is the projection of variables from the flux grids to the numerical boundary (and source) data, while Equation (66) simply states that the flux $\lambda_{j,i}$ between the fault and its surroundings should satisfy the semilocal Darcy's law. In the following section, we present the strategy for implementation of this approach and give details for a specific numerical scheme.

3.2 | MPFA discretization

It is of interest to consider the requirements put on the subdomain solution operators $\mathcal{S}_i$ in some more detail. From the variational formulations stated above, we see that for a discretization on a generic subdomain Ω_i to interact with the interface Γ_j, we need to provide operators which:

1. Handle Neumann boundary data on the form $\Pi_{N(\Omega_i)}\lambda_j$, for all interfaces Γ_j where Ω_i is the higher-dimensional neighbor.
2. Handle source terms $\Pi_{N(\Omega_i)}\lambda_j$ from interfaces Γ_j where Ω_i is the lower-dimensional neighbor.

3. Provide a discrete operator tr p_i so that $\Pi_{L^2(\Omega_i)}$ can project the pressure trace from $\partial_j\Omega_i$ to Γ_j where Ω_i is the higher-dimensional neighbor.
4. Provide a pressure p_i so that $\Pi_{L^2(\Omega_i)}$ can project the pressure to all Γ_j where Ω_i is the lower-dimensional neighbor.
5. Handle the divergence of vector source terms $\Pi_{N(\Omega_i)}(\nabla \cdot \boldsymbol{\mu}_{j,i})$ from interfaces Γ_j where Ω_i is the lower-dimensional neighbor.
6. Provide a pressure gradient u_i so that $\Pi_{L^2(\Omega_i)}$ can project the pressure gradient to all Γ_j where Ω_i is the lower-dimensional neighbor.

The four first requirements are readily available for any discretization scheme for elliptic equations. Specifically, we have based our solution operators on a cell-centered finite volume method termed the multipoint flux approximation (MPFA).[42,43] Treatment of vector source terms (item 5) is not as natural in primal discretization schemes such as finite elements, but is easy to include in most flux-based discretization methods such as, for example, mixed finite elements. We have employed the approach introduced in Starnoni et al.,[44] which treats the vector source term as part of the discrete divergence operator, and thereby provides an expression of the fluxes in terms of jumps in cell-centers vector sources. Finally, the pressure gradients are discretized as piece wise constant on each cell from an interpolation of the face cells fluxes (item 6). We implemented our model in PorePy, an open-source software for simulation of multiphysics processes in fractured porous media.[17]

To better understand the structure of the discrete coupling, it is instructive to write out the coupled system for two subdomains Ω_h and Ω_l separated by an interface Γ_j (see Figure 6). Let $\overline{p}_h$ and $\overline{p}_l$, be the vectors of cell-center pressures in Ω_h and Ω_l, respectively, and let $\overline{\lambda}_j$ be the vector of discrete mortar fluxes in Γ_j. The discrete coupled system in absence of external sources can then be represented on the generic form

$$\begin{bmatrix} A_h & 0 & G_h\Pi_{N(\Omega_h)} \\ 0 & A_l & B_l\Pi_{N(\Omega_l)} + J_l\Pi_{N(\Omega_l)}T_j \\ -\Pi_{L^2(\Omega_h)}P_h & \Pi_{L^2(\Omega_l)}P_l + T_j\Pi_{L^2(\Omega_l)}R_l & D_j \end{bmatrix} \begin{bmatrix} \overline{p}_h \\ \overline{p}_l \\ \overline{\lambda}_j \end{bmatrix} = \begin{bmatrix} 0 \\ 0 \\ 0 \end{bmatrix}. \tag{69}$$

The first two rows of the system (69) represent the discretized differential equations in each subdomain, while the third row is the discretized Darcy's law in the direction perpendicular to the interface. Here, A_h and A_l are the fixed-dimensional discretizations on the subdomains, G_h is the discretization of Neumann boundary conditions on Ω_h, B_l is the discretization of source terms in Ω_l, J_l is the discretization of the vector source term on Ω_l, T_j is the discretized $\mathfrak{K}_{\Omega\Gamma}\mathfrak{K}_{\Gamma\Gamma}^{-1}$ product on Γ_j, and $\Pi_{N(\Omega_h)}$ and $\Pi_{N(\Omega_l)}$ are the projection operators from coupling variables on the mortar grid to each of the subdomains degrees of freedom. Furthermore, P_h provides a discrete representation of the pressure trace operator on Ω_h, P_l gives the pressure unknowns on Ω_l, R_l gives the reconstruction of the pressure gradient on Ω_l, and $\Pi_{L^2(\Omega_k)}$ is the projection operator from numerical variables to coupling variables. Finally, D_j is the discretized inverse normal permeability on Γ_j.

We conclude by making two remarks: first, there is no direct coupling between Ω_h and Ω_l and second, global boundary conditions are left out of the system.

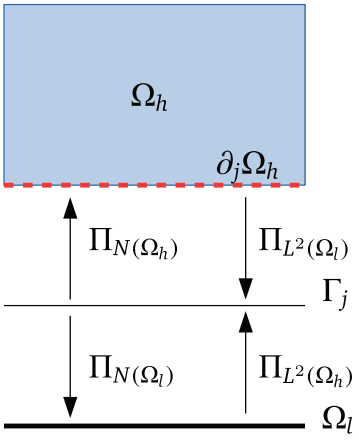

FIGURE 6 Illustration of a coupling between subdomains. Ω_h and Ω_l are the higher and lower subdomains, respectively, Γ_j is the interface between the two subdomains, $\partial_j\Omega_h$ is the portion of the boundary of Ω_h as seen from Γ_j, $\Pi_{N(\Omega_k)}$ is the projection operator from coupling variables on the mortar grid to each of the subdomains degrees of freedom ($k = h, l$), and $\Pi_{L^2(\Omega_k)}$ is the projection operator from numerical variables to coupling variables

4 | NUMERICAL EXAMPLES

We validate the semilocal model and our implementation by a suite of numerical examples. First, we consider a case with a single fault, and show how the semilocal model can capture the effects of anisotropic off-diagonal permeabilities, while the local model fails to do so. Second, we probe the robustness of our discretization on more complex geometries in 2D and 3D.

4.1 | Comparison to the equi-dimensional model

In this first example, we compare our reduced model to an equi-dimensional model. The aim is to highlight the enhanced modeling capabilities of our formulation with respect to the standard local formulation. With reference to this latter point, we present results of two test cases: the first one where the fault has the same off-diagonal permeability on both sides (see Figure 2B), and a second one where different permeability structures are assigned to each side of the fault (see Figure 2C).

4.1.1 | Case 1: Homogeneous permeability

We consider a 2D square domain of side $L = 1$ m cut by a horizontal fault of aperture $a = 1$ cm located in the middle of the domain. In the mixed-dimensional setting we therefore have two 2D domains Ω_1 and Ω_2 and one 1D fault Ω_3, as shown in Figure 7. The hydraulic conductivity is isotropic homogeneous for the 2D matrix, that is $\boldsymbol{K}_j = K_j\mathbf{I}$, with $j = 1, 2$, while for the fault we consider the following equi-dimensional full tensor:

$$\boldsymbol{K}_3 = \begin{bmatrix} K_{f,\parallel} & k_{f,t} \\ k_{f,t} & k_{f,\perp} \end{bmatrix}, \tag{70}$$

For simplicity, we take $K_1 = K_2 = K_m$. Boundary conditions consist of an applied difference in hydraulic head along the vertical direction and no-flow conditions elsewhere. In particular, the inlet pressure h_{in} is specified on the portion of the bottom boundary where $0.25 < x < 0.75$ m, while the outlet pressure h_{out} is specified on the portion of the top boundary where $x < 0.25$ & $x > 0.75$ m (see Figure 7). Data for the simulations are reported in Table 1. We consider as reference solution the solution obtained with an equi-dimensional model of $N = 40k$ structured square cells (mesh size $dx = 5$ mm), where the fault is discretized with two rows of 200 elements each. Then, for the reduced models, we consider triangular grids with approximately $N = [40, 160, 700, 3k, 11k]$ (respectively, $N_f = [4, 8, 16, 32, 64]$ cells for the fault), and report the average L^2 error in pressure along the fault

$$\varepsilon_p = \frac{\sqrt{\sum_i \Delta_i (p_i - p_{i,\text{eq}})^2}}{\sqrt{\sum_i \Delta_i p_{i,\text{eq}}^2}}, \tag{71}$$

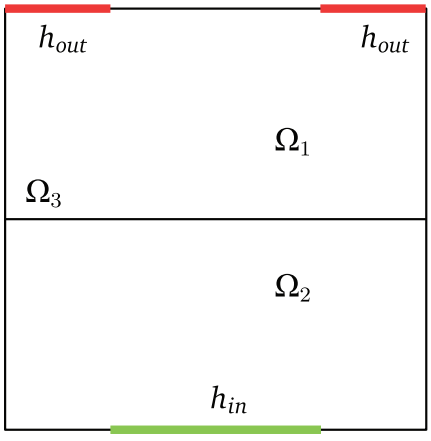

FIGURE 7 Setup of Case 1

where Δ_i is the size of the fault element in the reduced model, and $p_{i,\mathrm{eq}}$ is calculated from the equi-dimensional model as the mean value of the two fault cells at each location x_i:

$$p_{i,\mathrm{eq}}(x_i) = \sum_{j=y_1,y_2} p_{ij}, \tag{72}$$

where $y_j = L/2 \pm dx/2$.

Convergence results are shown in Figure 8(A). As Figure 8(A) clearly shows, our formulation presents about first-order convergence rate, while the local formulation does not converge. This is due to the strong anisotropy of the fault, which is not captured by the standard local formulation. As a result of the anisotropy of the fault, the flow will take a preferential direction towards one of the two inlets, therefore breaking the symmetry of the local formulation. This is better observed in Figure 8(B) showing the pressure distribution along the fault for the three models. As Figure 8(B) clearly shows, the semilocal and the equi-dimensional models coincide, while the local formulation exhibits an erroneous symmetric profile. We remark that, following Gander et al.,[12] one would expect that both the semilocal and local model solutions converge to the equi-dimensional solution for $a \to 0$ (when keeping the material parameters constant). As already discussed in the Introduction, this is consistent with the fact that local laws might provide sufficiently accurate solutions for fractures, however, they fail for highly anisotropic fault zones.

TABLE 1 Data for Case 1

Parameter	Description	Value
K_m	Matrix hydraulic conductivity	1 m/s
$K_{f,\parallel}$	Fault tangential hydraulic conductivity	100 m/s
$k_{f,\perp}$	Fault normal hydraulic conductivity	100 m/s
$k_{f,t}$	Fault off-diagonal hydraulic conductivity	80 m/s
a	Fault aperture	0.01 m
L	Side of the square domain	1 m
h_{in}	Hydraulic head at the bottom boundary	10 m
h_{out}	Hydraulic head at the top boundary	1 m

Note: Values of the fault hydraulic conductivity are given for the equi-dimensional model, that is, before scaling.

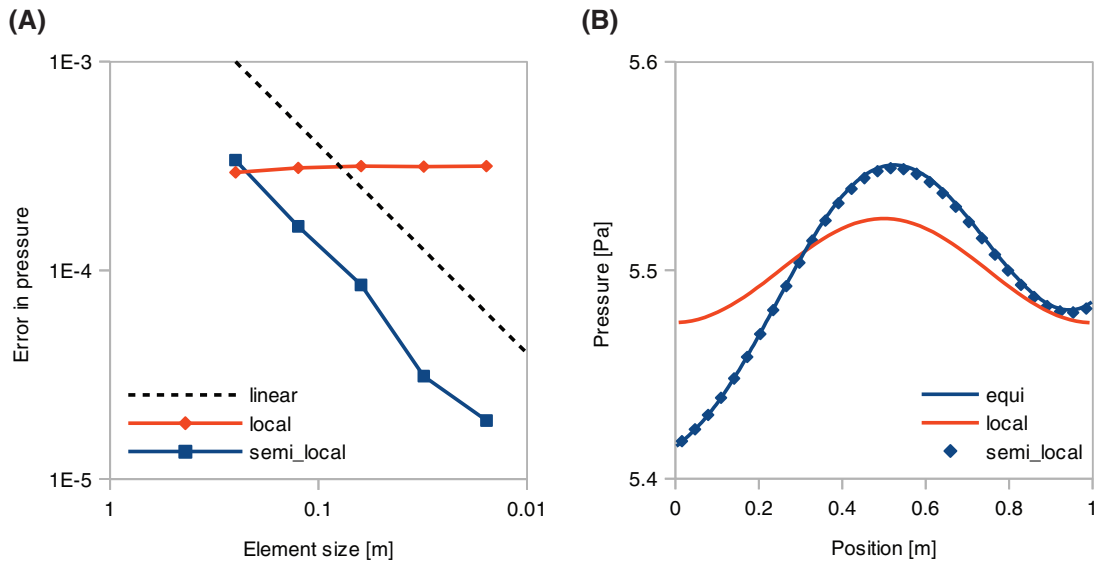

FIGURE 8 Case 1: (A) Convergence of the average error in pressure within the fault and (B) pressure distribution along the fault for different methods

4.1.2 | Case 2: Dual permeability

As a further illustration of the enhanced modeling capabilities of the semilocal model, we modify the setup used in the previous section to have different permeability structures on the two sides of the fault. This is relevant for modeling of geological faults, where the two sides of the fault may undergo different damage processes. To that end, we divide the fault into an upper and lower part (see Figure 9) and assign different permeability structures to the two sides, that is for $j = 1, 2$:

$$\boldsymbol{K}_{3,j} = \begin{bmatrix} K_{f,\parallel} & k_{f,j,t} \\ k_{f,j,t} & k_{f,\perp} \end{bmatrix}. \tag{73}$$

In particular, values of K_m, $K_{f,\parallel}$, and $k_{f,\perp}$ are the same as those given in Table 1, while $k_{f,1,t}$ and $k_{f,2,t}$ take values of 50 and 80 m/s, respectively. The aperture of the fault is set to $a = 2$ cm and we use the same boundary conditions as in Case 1.

Convergence results for the local and semilocal models are shown in Figure 10(A,B), with the reference solution again computed from an equi-dimensional model with a grid with 40k cells. As in the previous case, the local model fails to converge, while the semilocal model exhibits first-order convergence up to the last refinement step. Here, the mesh size is of the same order of the fault aperture, thus further error reduction cannot be expected due to the modeling error in the dimension reduction.

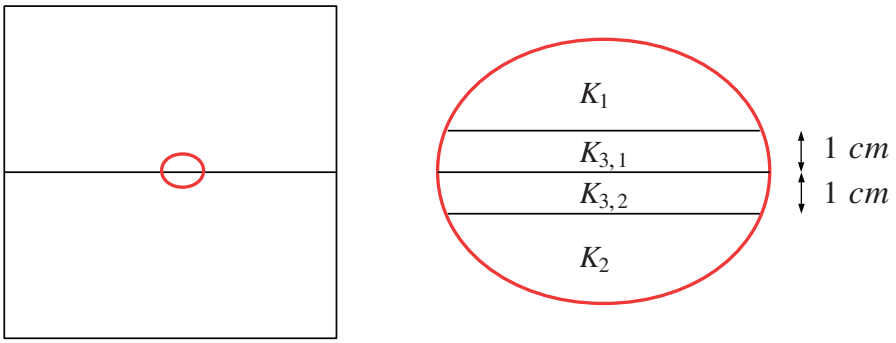

FIGURE 9 Setup of Case 2

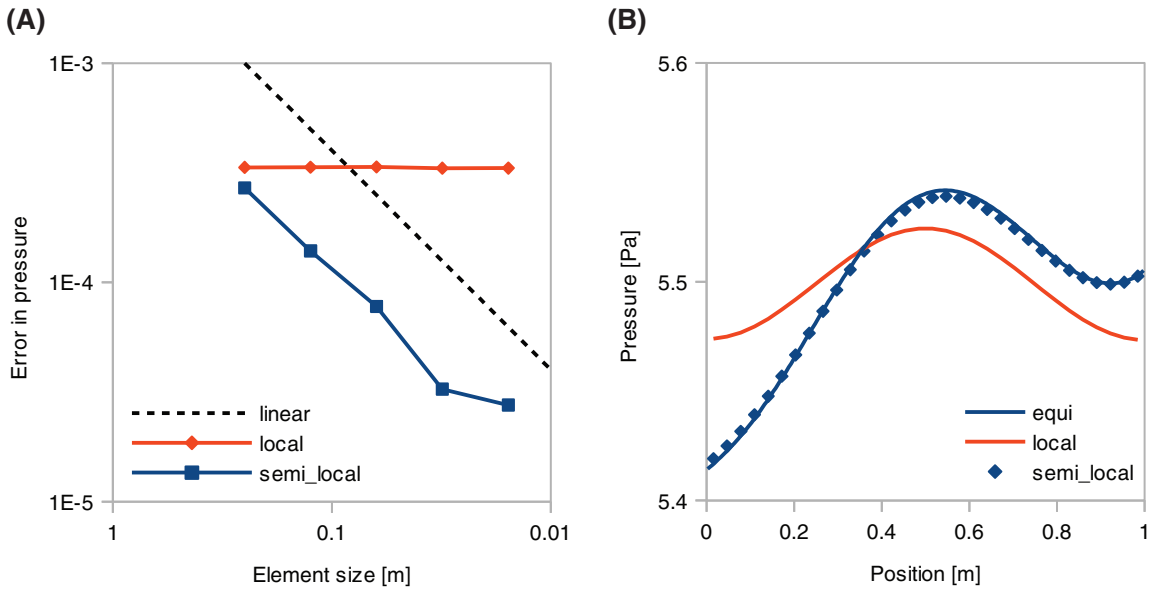

FIGURE 10 Case 2: (A) Convergence of the average error in pressure within the fault and (B) pressure distribution along the fault for different methods

4.2 | Self-convergence

In this section, we test the robustness of the method on more challenging fault configurations in 2D and 3D. We remark that no equi-dimensional solutions are available for these tests, and that this subsection aims at observing the numerical scheme's order of convergence.

4.2.1 | 2D case

We consider the same test case as Case 1 in Boon et al.[10] The domain is a unit square including a network of five faults (Figure 11A). Of these five faults, one cuts the square domain into two 2D subdomains, denoted as Ω_1 and Ω_2, respectively. The faults are numbered for $j = 3, .., 7$ and are of two kinds: Ω_3 and Ω_4 are conductive, that is $K_3 = K_4 = K_{f,1}$, while the other three are blocking, that is $K_5 = K_6 = K_7 = K_{f,2}$. The hydraulic conductivity is isotropic homogeneous for the 2D matrix, with $K_1 = K_2 = K_m$, while for the faults we consider an equi-dimensional full tensor with $k_{j,t} = 0.1K_{j,\|}$, for $j = 3, .., 7$. Boundary conditions consist of an applied difference in hydraulic head along the vertical direction and no-flow conditions elsewhere. Data for the simulations are reported in Table 2. We consider as reference solution the solution obtained with approximately $N = 133k$ cells for the 2D domain and a total number of $N_f = 510$ cells for the faults. Then we consider grids with approximately $N = [300, 1k, 4k, 17k, 67k]$ (respectively, $N_f = [26, 48, 93, 183, 363]$), and report the average L^2 error in pressure along the faults.

The convergence results, shown in Figure 11(B), indicate a rate of at least first order. The test thus confirms the performance of our method also in cases that involve faults that are intersecting and have low permeability. Both these features are highly relevant in a geologic setting where fault may have complex geometry and reduced permeability compared with the host rock.

4.2.2 | 3D case

As a final verification, we consider a 3D case with multiple intersecting faults. The setup is based on Case 2 in the benchmark study described in Reference 40. The domain is a unit cube including a network of nine faults, whose intersections divide the cubic domain into several subdomains, as shown in Figure 12(A). These 3D subdomains are grouped into two regions, where we assigned different permeabilities $K_{m,1}$ and $K_{m,2}$, both homogeneous and isotropic (see Reference 40 for a visualization of these two regions). For the faults we consider full tensors with tangential permeability $\boldsymbol{K}_{j,\|} = K_{f,\|}\mathbf{I}_{\|}$,

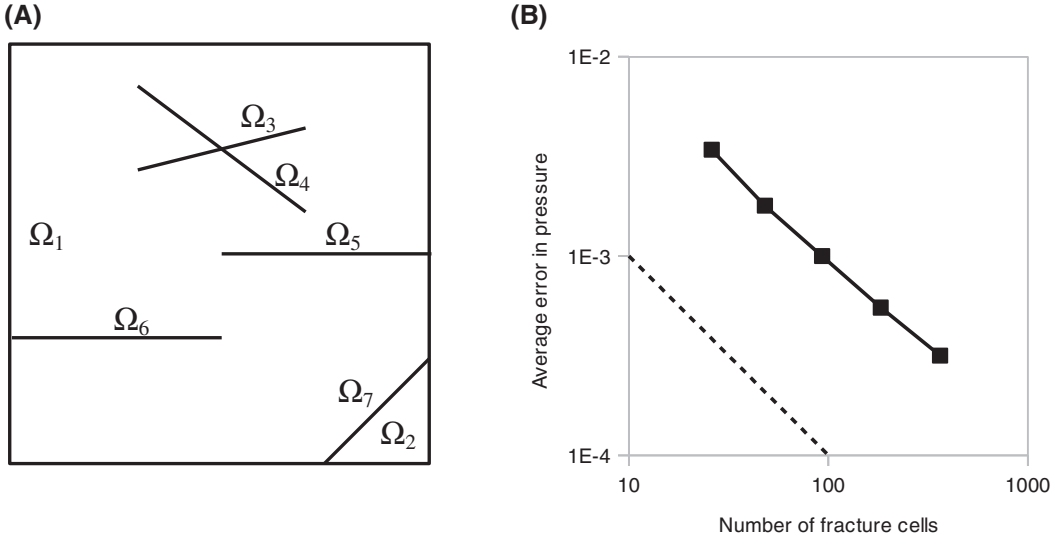

FIGURE 11 Two-dimensional self-convergence test: (A) Mixed-dimensional geometry and (B) convergence of the average error in pressure within the faults

TABLE 2 Data for the two-dimensional self-convergence test

Parameter	Description	Value
K_m	Matrix hydraulic conductivity	1 m/s
$K_{f,1,\parallel}$	Fault tangential hydraulic conductivity	100 m/s
$k_{f,1,\perp}$	Fault normal hydraulic conductivity	100 m/s
$k_{f,1,t}$	Fault off-diagonal hydraulic conductivity	10 m/s
$K_{f,2,\parallel}$	Fault tangential hydraulic conductivity	0.01 m/s
$k_{f,2,\perp}$	Fault normal hydraulic conductivity	0.01 m/s
$k_{f,2,t}$	Fault off-diagonal hydraulic conductivity	0.001 m/s
a	Fault aperture	0.01 m
h_{in}	Hydraulic head at the top boundary	1 m
h_{out}	Hydraulic head at the bottom boundary	0 m

Note: Values of the fault hydraulic conductivity are given for the equi-dimensional model, that is, before scaling.

FIGURE 12 Three-dimensional self-convergence test: (A) Mixed-dimensional geometry and (B) convergence of the average error in pressure within the faults

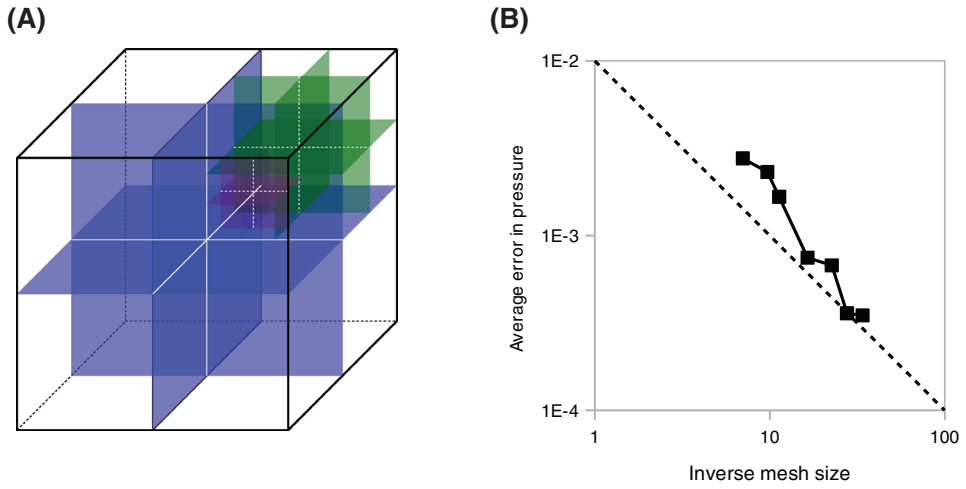

TABLE 3 Data for the three-dimensional self-convergence test

Parameter	Description	Value
$K_{m,1}$	Matrix hydraulic conductivity	1 m/s
$K_{m,2}$	Matrix hydraulic conductivity	0.1 m/s
$K_{f,\parallel}$	Fault tangential hydraulic conductivity	$1e^4$ m/s
$k_{f,\perp}$	Fault normal hydraulic conductivity	$1e^4$ m/s
$k_{f,t}$	Fault off-diagonal hydraulic conductivity	$1e^3$ m/s
a	Fault aperture	$1e^{-4}$ m
q_{in}	Normal flux at the inflow boundary	−1 m/s
h_{out}	Hydraulic head at the outflow boundary	1 m

Note: Values of the fault hydraulic conductivity are given for the equi-dimensional model, that is, before scaling.

normal permeability $k_{j,\perp} = k_{f,\perp}$, and off-diagonal permeability $\boldsymbol{k}_{j,t} = 0.1 k_{j,t} \mathbf{i}_{\|}$. Boundary conditions consist of an imposed normal flux q_{in} on the portion of the boundary where $(x, y, z) < 0.25$ m and a constant hydraulic head h_{out} on the portion of the boundary where $(x, y, z) > 0.875$ m. Data for the simulations are reported in Table 3. We consider as reference solution the solution obtained with approximately $N_3 = 85k$ cells for the 3D domain and a total number of $N_f = 8364$ cells for all faults. Then we consider $N_3 = [500, 1k, 2k, 4k, 10k, 20k, 40k]$ (respectively, $N_f = [148, 282, 384, 814, 1536, 2298, 3456]$) and report the average L^2 error in pressure along the faults.

Convergence results are shown in Figure 12(B), indicating first-order convergence on average. This confirms the consistency of our implementation also for 3D problems with complex fault geometries.

5 | CONCLUSIONS

We presented an improved framework to modeling and discretizing flow in generally anisotropic porous media with thin inclusions, within the context of mixed-dimensional partial differential equations. Our model considers a full permeability tensor for the inclusions, resulting in additional terms arising in our formulation as compared with existing local discretizations. We expect our model to be important for modeling of flow in faulted porous media, however, the methods proposed herein can be in any case applied to models of fractures, in fact our full-permeability model naturally reduces to the existing models of fracture-matrix flow when the off-diagonal components of the inclusion permeability tensor are set to zero.

We provided numerical examples showing convergence of the method for both 2D and 3D faulted porous media. In particular, we provided numerical evidence that, as opposed to existing local discretizations, our model is capable of simulating the anisotropic behavior of the faults near damage zone.

We remark that, in the spirit of flux-mortars coupling schemes, our formulation is independent of the discretization methods used to discretize the flow equations in the porous matrix and the faults. However, we only showed results obtained using a multipoint flux finite volume approach. Nevertheless, the formulation also applies to other discretization methods, for example, mixed finite elements.

ACKNOWLEDGMENT

This work forms part of Norwegian Research Council project 250223.

DATA AVAILABILITY STATEMENT

The data that support the findings of this study are available from the corresponding author upon reasonable request.

ORCID

Michele Starnoni https://orcid.org/0000-0002-8552-6997

REFERENCES

1. Bödvarsson GS, Tsang CF. Injection and thermal breakthrough in fractured geothermal reservoirs. *J Geophys Res Solid Earth*. 1982;87(B2):1031-1048.
2. Cao P, Liu J, Leong Y-K. A fully coupled multiscale shale deformation-gas transport model for the evaluation of shale gas extraction. *Fuel*. 2016;178:103-117.
3. Johnson SM, Morris JP. Hydraulic fracturing mechanisms in carbon sequestration applications. Paper presented at: Proceedings of the 43rd US Rock Mechanics Symposium & 4th US-Canada Rock Mechanics Symposium. American Rock Mechanics Association: Asheville, North Carolina; 2009.
4. Nagelhout ACG, Roest JPA. Investigating fault slip in a model of an underground gas storage facility. *Int J Rock Mech Min Sci*. 1997;34(3-4):212-e1.
5. Oda M. Permeability tensor for discontinuous rock masses. *Geotechnique*. 1985;35(4):483-495.
6. Farmer CL. Upscaling: a review. *Int J Numer Methods Fluids*. 2002;40(1-2):63-78.
7. Liu R, Li B, Jiang Y, Huang N. Mathematical expressions for estimating equivalent permeability of rock fracture networks. *Hydrogeol J*. 2016;24(7):1623-1649.
8. Sævik PN, Berre I, Jakobsen M, Lien M. A 3d computational study of effective medium methods applied to fractured media. *Transp Porous Media*. 2013;100(1):115-142.
9. Martin V, Jaffré J, Roberts JE. Modeling fractures and barriers as interfaces for flow in porous media. *SIAM J Sci Comput*. 2005;26(5):1667-1691.

10. Boon WM, Nordbotten JM, Yotov I. Robust discretization of flow in fractured porous media. *SIAM J Numer Anal*. 2018;56(4): 2203-2233.
11. Nordbotten JM, Boon WM, Fumagalli A, Keilegavlen E. Unified approach to discretization of flow in fractured porous media. *Comput Geosci*. 2019;23(2):225-237.
12. Gander MJ, Hennicker J, Masson R. Modeling and analysis of the coupling in discrete fracture matrix models. *SIAM J Numer Anal*. 2021;59(1):195-218.
13. Karimi-Fard M, Durlofsky LJ, Aziz K, et al. An efficient discrete fracture model applicable for general purpose reservoir simulators. Paper presented at: Proceedings of the SPE Reservoir Simulation Symposium. Society of Petroleum Engineers: Houston, Texas; 2003.
14. Sandve TH, Berre I, Nordbotten JM. An efficient multi-point flux approximation method for discrete fracture–matrix simulations. *J Comput Phys*. 2012;231(9):3784-3800.
15. Schwenck N, Flemisch B, Helmig R, Wohlmuth BI. Dimensionally reduced flow models in fractured porous media: crossings and boundaries. *Comput Geosci*. 2015;19(6):1219-1230.
16. Formaggia L, Fumagalli A, Scotti A, Ruffo P. A reduced model for Darcy's problem in networks of fractures. *ESAIM Math Modell Numer Anal*. 2014;48(4):1089-1116.
17. Keilegavlen E, Berge R, Fumagalli A, et al. Porepy: an open-source software for simulation of multiphysics processes in fractured porous media. *Comput Geosci*. 2021;25(1):243-265. https://doi.org/10.1007/s10596-020-10002-5.
18. Angot P, Boyer F, Hubert F. Asymptotic and numerical modelling of flows in fractured porous media. *ESAIM Math Modell Numer Anal*. 2009;43(2):239-275.
19. Brenner K, Groza M, Guichard C, Lebeau G, Masson R. Gradient discretization of hybrid dimensional Darcy flows in fractured porous media. *Numer Math*. 2016;134(3):569-609.
20. Brenner K, Hennicker J, Masson R, Samier P. Gradient discretization of hybrid-dimensional Darcy flow in fractured porous media with discontinuous pressures at matrix–fracture interfaces. *IMA J Numer Anal*. 2017;37(3):1551-1585.
21. Reichenberger V, Jakobs H, Bastian P, Helmig R. A mixed-dimensional finite volume method for two-phase flow in fractured porous media. *Adv Water Resour*. 2006;29(7):1020-1036.
22. Brenner K, Groza M, Guichard C, Masson R. Vertex approximate gradient scheme for hybrid dimensional two-phase Darcy flows in fractured porous media. *ESAIM Math Modell Numer Anal*. 2015;49(2):303-330.
23. Brenner K, Hennicker J, Masson R, Samier P. Hybrid-dimensional modelling of two-phase flow through fractured porous media with enhanced matrix fracture transmission conditions. *J Comput Phys*. 2018;357:100-124.
24. Bear J. *Hydraulics of Groundwater*. New York, NY: Mc GrawHill Inc; 1979.
25. Yortsos YC. A theoretical analysis of vertical flow equilibrium. *Transp Porous Media*. 1995;18(2):107-129.
26. Nordbotten JM, Celia MA. *Geological Storage of CO2: Modeling Approaches for Large-Scale Simulation*. Hoboken, NJ: John Wiley & Sons; 2011.
27. Březina J, Stebel J. Analysis of model error for a continuum-fracture model of porous media flow. Paper presented at: Proceedings of the International Conference on High Performance Computing in Science and Engineering; 2015:152-160; Springer, New York, NY.
28. Armiti-Juber A, Rohde C. Existence of weak solutions for a nonlocal pseudo-parabolic model for brinkman two-phase flow in asymptotically flat porous media. *J Math Anal Appl*. 2019;477(1):592-612.
29. Kumar K, List F, Pop I, Radu F. Formal upscaling and numerical validation of fractured flow models for Richards equation. *J Comput Phys*. 2019;407:109138.
30. Fossen H, Schultz RA, Shipton ZK, Mair K. Deformation bands in sandstone: a review. *J Geol Soc*. 2007;164(4):755-769.
31. Fossen H, Johansen TES, Hesthammer J, Rotevatn A. Fault interaction in porous sandstone and implications for reservoir management; examples from southern Utah. *AAPG Bull*. 2005;89(12):1593-1606.
32. Johansen TES, Fossen H. Internal geometry of fault damage zones in interbedded siliciclastic sediments. *Geol Soc Lond Spec Publ*. 2008;299(1):35-56.
33. Hesthammer J, Johansen TES, Watts L. Spatial relationships within fault damage zones in sandstone. *Mar Pet Geol*. 2000;17(8): 873-893.
34. Fumagalli A, Scotti A. A multi-layer reduced model for flow in porous media with a fault and surrounding damage zones; 2019. arXiv preprint arXiv:1903.01117.
35. Wilson P, Smith S, Povey D, Harris S. Ranking and selecting fault models using flow-indicator fault properties and simple streamline simulations. *Pet Geosci*. 2020;27(2):petgeo2020-017.
36. Helmig R. *Multiphase flow and Transport Processes in the Subsurface: A Contribution to the Modeling of Hydrosystems*. New York, NY: Springer-Verlag; 1997.
37. Fumagalli A, Keilegavlen E. Dual virtual element methods for discrete fracture matrix models. *Oil & Gas Sci Technol–Revue d'IFP Energies nouvelles*. 2019;74:41.
38. Formaggia L, Scotti A, Sottocasa F. Analysis of a mimetic finite difference approximation of flows in fractured porous media. *ESAIM Math Modell Numer Anal*. 2018;52(2):595-630.
39. Flemisch B, Berre I, Boon W, et al. Benchmarks for single-phase flow in fractured porous media. *Adv Water Resour*. 2018;111: 239-258.
40. Berre I, Boon WM, Flemisch B, et al. Verification benchmarks for single-phase flow in three-dimensional fractured porous media. *Adv Water Resour*. 2020;147:103759.

41. Boon WM, Nordbotten JM, Vatne JE. Functional analysis and exterior calculus on mixed-dimensional geometries. *Annali di Mathematica*. 2021;200:757-789.
42. Aavatsmark I. An introduction to multipoint flux approximations for quadrilateral grids. *Comput Geosci*. 2002;6(3-4): 405-432.
43. Nordbotten JM, Keilegavlen E. An introduction to multi-point flux (mpfa) and stress (mpsa) finite volume methods for thermo-poroelasticity; 2020. arXiv preprint arXiv:2001.01990.
44. Starnoni M, Berre I, Keilegavlen E, Nordbotten JM. Consistent mpfa discretization for flow in the presence of gravity. *Water Resour Res*. 2019;55(12):10105-10118.

How to cite this article: Starnoni M, Berre I, Keilegavlen E, Martin Nordbotten J. Modeling and discretization of flow in porous media with thin, full-tensor permeability inclusions. *Int J Numer Methods Eng*. 2021;122:4730–4750. https://doi.org/10.1002/nme.6744